Cell Biomaterials

Article

Replacing extraocular muscles with anisotropic, strain-stiffening hydrogels

Graphical abstract

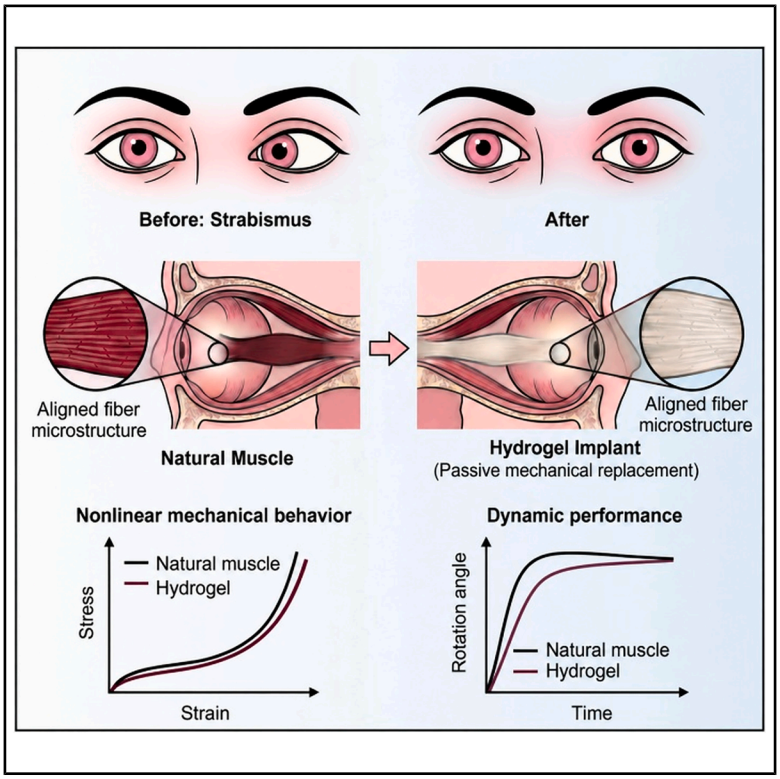

Highlights

- Hierarchical processing creates hydrogels with anisotropic strain-stiffening behavior
- The hydrogel resists fatigue and matches the passive stiffness of extraocular muscles
- Implantation in a rabbit model eliminates pathological over-rotation

Authors

Chuan Wei Zhang, Yingjie Du, Ruoyi Ke, ..., Federico G. Velez, Stacy L. Pineles, Ximin He

Correspondence

FVelez@mednet.ucla.edu (F.G.V.), SPineles@mednet.ucla.edu (S.L.P.), ximinhe@ucla.edu (X.H.)

In brief

Natural extraocular muscles are compliant at small strains to permit rapid rotation, but stiffen at large strains to prevent over-rotation. Conventional surgeries cannot restore this passive mechanical signature in paralyzed muscles. We report a hierarchically structured hydrogel that replicates the J-shaped stress-strain response of native muscle. Implanted in rabbits, the hydrogel restores physiological eye rotation dynamics.

Zhang et al., 2027, Cell Biomaterials *3*, 100595
May 18, 2027
https://doi.org/10.1016/j.celbio.2026.100595

CellPress

Please cite this article in press as: Zhang et al., Replacing extraocular muscles with anisotropic, strain-stiffening hydrogels, Cell Biomaterials (2026), https://doi.org/10.1016/j.celbio.2026.100595

Cell Biomaterials

CellPress
OPEN ACCESS

Article

Replacing extraocular muscles with anisotropic, strain-stiffening hydrogels

Chuan Wei Zhang,[1,5] Yingjie Du,[1,5] Ruoyi Ke,[1,5] Wen Hong,[1] Zixiao Liu,[1] Dongmin Yoon,[1] Mason Possinger,[1] Chi Chen,[1] Hua Zhou,[3] Yangzhi Zhu,[4] Federico G. Velez,[2,*] Stacy L. Pineles,[2,*] and Ximin He[1,6,*]

[1]Department of Materials Science and Engineering, University of California, Los Angeles, Los Angeles, CA 90095, USA
[2]Stein Eye Institute and Department of Ophthalmology, University of California, Los Angeles, Los Angeles, CA 90095, USA
[3]Advanced Photon Source, Argonne National Laboratory, Lemont, IL 60439, USA
[4]Biomedical Device Center, Terasaki Institute for Biomedical Innovation, Los Angeles, CA 90024, USA
[5]These authors contributed equally
[6]Lead contact
*Correspondence: FVelez@mednet.ucla.edu (F.G.V.), SPineles@mednet.ucla.edu (S.L.P.), ximinhe@ucla.edu (X.H.)
https://doi.org/10.1016/j.celbio.2026.100595

THE BIGGER PICTURE Strabismus surgery faces a fundamental limit: it corrects alignment at the cost of mechanics. To align the eye, surgeons must detach and move muscles. This alters the native length-tension relationship: recession creates slack that delays movement, while resection imposes pre-stretch that restricts rotation. Furthermore, for patients with paralyzed or fibrotic muscles, surgery cannot restore the missing passive tension required to stabilize the eye. Synthetic implants offer an alternative, but they must match the specific passive mechanics of the natural tissue: compliant at small strains for rapid motion, yet stiff at large strains to prevent over-rotation. We demonstrate that a hydrogel engineered to replicate this specific stress-strain profile can function as a passive muscle replacement. By restoring the physiological passive constraint rather than just repositioning attachments, this work offers a strategy to treat complex strabismus without compromising eye dynamics.

SUMMARY

Strabismus surgeries rely on weakening or tightening extraocular muscles. While effective for alignment, these procedures disrupt the length-tension relationships. Recession induces slack, causing delayed force transmission; resection induces stretch, increasing passive drag. Neither technique can augment a muscle that has lost function due to paralysis or atrophy. An implant must replace the passive constraint of the natural muscle. Here, we report a hydrogel implant that replicates the passive mechanics of extraocular muscles. We fabricate the hydrogel through a four-step hierarchy: directional freezing for alignment, salting-out for density, mechanical training for the J-shaped stress-strain curve, and chemical crosslinking for stability. The hydrogel reproduces native tissue's J-shaped stress-strain response and resists fatigue. In a rabbit model of lateral rectus deficiency, the implant restores physiological rotation ranges ($\sim$25°) and saccade velocities, avoiding pathological over-rotation after muscle removal. This work establishes passive muscle replacement as a therapeutic strategy, restoring alignment while preserving physiological dynamics.

INTRODUCTION

Extraocular muscles coordinate eye movements through a precise balance of active contraction and passive tension. Strabismus disrupts this balance, affecting 2%–5% of the global population and impairing binocular vision.[1–4] Surgeons currently realign eyes by altering muscle length or attachment: recession loosens an overactive muscle, while resection tightens an underactive one (Figure 1A).[5,6] However, these procedures compromise the native length-tension relationship of the muscle. Recession creates slack that delays force transmission; resection imposes restrictive drag.[7,8] Consequently, the eyes often fail to move in coordination across all gaze directions.[9,10] A more severe limitation arises in conditions such as paralytic strabismus or congenital fibrosis, where the muscle loses both active contraction and passive elastic tension, leaving the eye without the elastic constraint that prevents over-rotation.[11–13] Existing surgeries cannot restore this lost passive mechanical support. Without this support, the eye suffers pathological over-rotation due to the unopposed pull of the antagonist muscle. Although natural muscles are active actuators, their passive stiffness is equally critical for ocular stability. Restoring this

Please cite this article in press as: Zhang et al., Replacing extraocular muscles with anisotropic, strain-stiffening hydrogels, Cell Biomaterials (2026), https://doi.org/10.1016/j.celbio.2026.100595

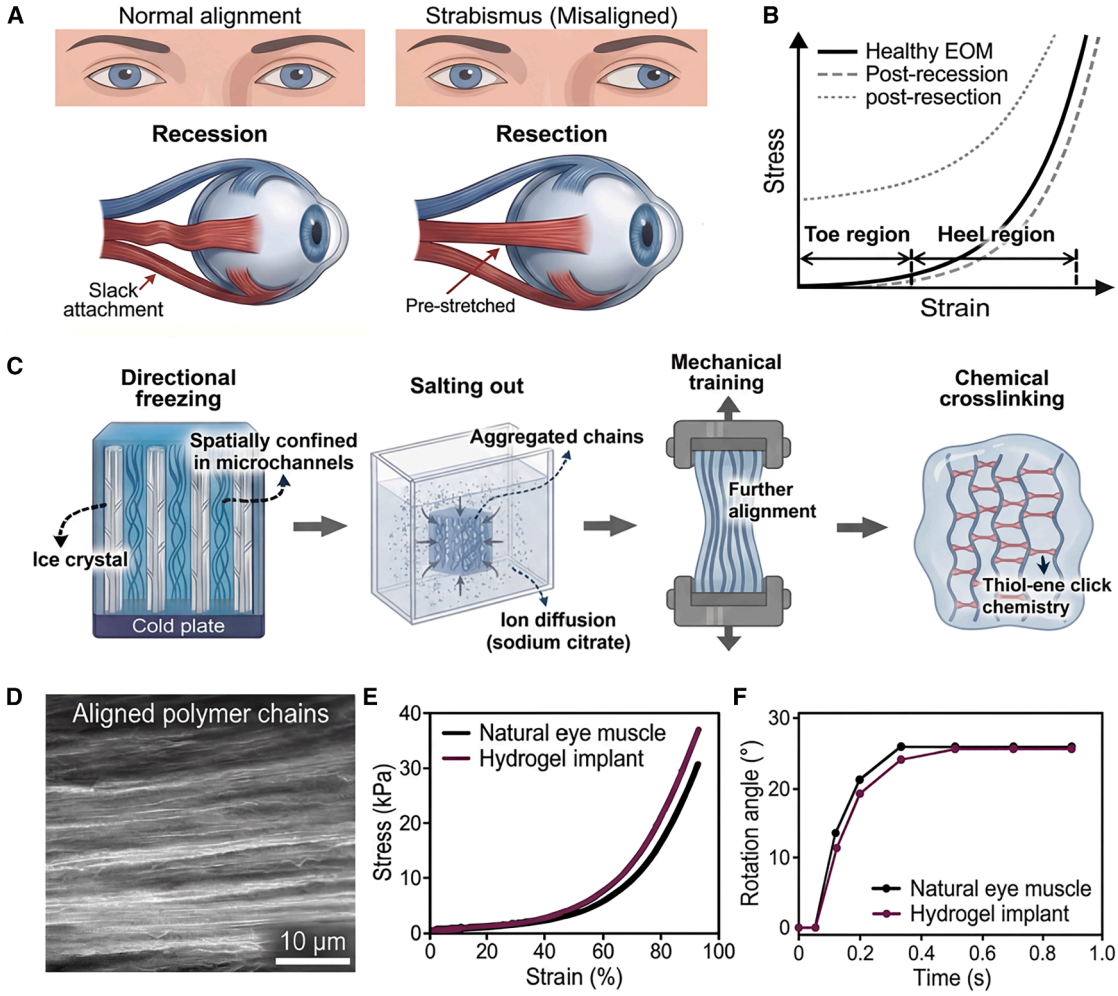

Figure 1. Design of a passive muscle

(A) Mechanical disruption after conventional surgery. Slack after recession and passive drag after resection.

(B) Nonlinear mechanical target. Low-strain compliance for rapid motion and high-strain stiffening at the rotational limit (J-curve).

(C) Hierarchical fabrication sequence. Polymer-chain alignment by directional freezing, network densification by salting-out, formation of aligned nanocrystalline domains by mechanical training, and structural locking by covalent crosslinking.

(D) Muscle-like microchannel alignment.

(E) Mechanical matching to native muscle. Reproduction of the natural-muscle J-curve by the hydrogel.

(F) Functional restoration by the passive implant. Recovery of saccade dynamics in a rabbit model.

passive constraint is essential to prevent over-rotation. Therefore, a clinical solution must go beyond static realignment; it must mechanically replace the weakened muscle.

An ideal implant must replicate the passive mechanics of the native muscle.[14–16] The extraocular muscle functions as a nonlinear spring: it is compliant at small strains to permit rapid eye rotation but stiffens sharply at large strains to act as a check ligament. This J-shaped stress-strain behavior balances mobility with stability (Figure 1B).[17] Current clinical materials, such as silicone, fail to mimic this nonlinearity.[18–20] Conventional silicone elastomers behave approximately as neo-Hookean solids and lack the strain-stiffening response of biological tissues. Although architectural engineering can render silicone networks strain stiffening,[21] such hydrophobic systems differ fundamentally in molecular constitution from the predominantly aqueous biological tissues they would replace, with implications for potential mass transport, lubrication, and tissue integration. Hydrogels offer a tissue-like constitution.[22–27] Among them, poly(vinyl alcohol) (PVA) offers a uniquely suitable combination of established biocompatibility, broadly tunable mechanical properties via the Hofmeister effect, and processing-controlled nonlinear stress-strain behavior.[26,27] The challenge is not merely to synthesize a tough hydrogel but to engineer a material that reproduces the J-curve of the extraocular muscle while surviving the relentless dynamic environment of the orbit.[17,28–30] The implant must endure thousands of saccades daily without fatigue failure or creep.[31–34] Meeting both demands requires hierarchical engineering that no single processing step can deliver.

Here we report a hydrogel implant engineered to recapitulate the passive mechanics of extraocular muscles. We achieve the

Please cite this article in press as: Zhang et al., Replacing extraocular muscles with anisotropic, strain-stiffening hydrogels, Cell Biomaterials (2026), https://doi.org/10.1016/j.celbio.2026.100595

requisite anisotropy, nonlinearity, and fatigue resistance through a hierarchical fabrication strategy (Figure 1C). First, directional freezing organizes polymer chains into aligned microchannels, mimicking the anisotropic alignment of native muscle fibers. Second, salting-out densifies the network via the Hofmeister effect, tuning the elastic modulus to the physiological range. Third, mechanical training induces aligned nanocrystalline domains that act as physical crosslinks, tuning the J-shaped strain-stiffening behavior essential for balancing mobility and stability. Fourth, thiol-ene click chemistry introduces covalent crosslinks that stabilize the aligned structure for operation in the dynamic orbital environment. The resulting hydrogel reproduces the passive length-tension relationship of healthy muscles. Finite element simulations confirm that this mechanical matching restores physiological eye rotation dynamics. In a rabbit model of lateral rectus deficiency, the implant restores the range of motion and saccade velocities (510°/s) to near-normal levels, effectively preventing the pathological over-rotation observed in the absence of mechanical support. Histological analysis supports short-term tissue compatibility with stable fibrous encapsulation. This work establishes passive muscle replacement as a viable therapeutic strategy, demonstrating that restoring the passive mechanics of a tissue can normalize physiological eye dynamics in lateral rectus deficiency.

RESULTS

Mimicking passive mechanics

We engineer the hydrogel through a hierarchy of four processes, where each step targets a specific physical attribute (Figure 1C). Directional freezing aligns polymer chains into microchannels, creating the anisotropic structure. Salting-out densifies the network via the Hofmeister effect, tuning the modulus to the physiological range.[35] Mechanical training stretches the polymer chains, inducing the J-shaped strain-hardening behavior. Covalent crosslinking locks the aligned structure via thiol-ene click chemistry, ensuring fatigue resistance. The sequence of these steps is as critical as the steps themselves (Figure S1). Crosslinking prior to training suppresses chain reorientation, yielding an isotropic, excessively stiff network. Training prior to crosslinking allows the chains to reorient and extend freely. We therefore adopt the sequence of directional freezing, mechanical training, and chemical crosslinking (DF-MT-C). This strategy maximizes the alignment and strain-hardening capacity before the covalent network permanently locks the topology.

Scanning electron microscopy reveals the structural basis of the design: aligned polymer fibers that mimic the anisotropic structure of native muscle (Figure 1D). The hydrogel further exhibits training-induced anisotropy in two-dimensional (2D) small-angle X-ray scattering (SAXS): after mechanical training, the scattering halo becomes anisotropic and the corresponding azimuthal intensity profile develops pronounced peaks (Figure S2). This anisotropy governs the mechanical response (Figure S4). As the hydrogel stretches, the polymer chains uncoil and align, a process that sharply increases stiffness at high strains. This mechanism mirrors the recruitment of collagen fibers in biological tissues. This structural evidence validates the necessity of the processing sequence (DF-MT-C). Consequently, the hydrogel precisely recapitulates the J-shaped stress-strain curve of the extraocular muscle (Figure 1E). The material exhibits a compliant toe region to permit rapid rotation and transitions to a stiff heel region to provide passive constraint. This mechanical biomimicry translates directly into restoration of physiological eye dynamics. In a rabbit model, the hydrogel implant restores the saccade dynamics. The eye achieves the target rotation angle and stabilizes within ~300 ms, effectively eliminating the pathological overshoot observed in the absence of the muscle (Figure 1F).

Engineering the J-curve

We tune the processing parameters to achieve precise mechanical matching with the native tissue. The salting-out process regulates the network density and baseline stiffness. As the concentration of sodium citrate increases from 0.5–2.0 M, the Hofmeister effect progressively aggregates the polymer chains (Figure 2A). This densification enhances the strength monotonically from 47–220 kPa. We identify 1.5 M as the optimal concentration by comparing the salting-out-dependent stress-strain curves with the native extraocular-muscle J-curve measured in Figure 1E. Above this threshold, the modulus exceeds the physiological range, while below it, the network density is insufficient to support the J-curve. Thus, the 1.5 M condition best matches the native stress-strain target while maintaining a water content comparable to that of native muscles (Figures 2A and S3). Based on this composition, the mechanical training programs the nonlinearity. We vary the training strain to modulate the J-curve profile (Figure 2B). The training strain dictates the extent of chain alignment. A low training strain (50%) results in a nearly linear response, indicating insufficient anisotropy. By contrast, higher training strains (100%–200%) induce a sharp transition from a compliant toe region to a stiff heel region. The transition strain and the heel modulus are sensitive to the training history. We select a training strain of 150% to align the polymer chains and reproduce the J-curve of the extraocular muscle.

With the mechanical profile established by physical processing, we introduce chemical crosslinking to ensure stability. A purely physical network allows polymer chains to slip over time, leading to plastic deformation under cyclic loads. A covalent network is required to lock the network topology. However, excessive crosslinking restricts the chain straightening essential for the J-curve. We systematically vary the total (3-mercaptopropyl)triethoxysilane (MPTES)/vinyldimethylethoxysilane (VDMES) silane loading from 1.8 to 7.2 wt % (Figure 2C), defined as the combined silane feed relative to the mass of the 10 wt % PVA precursor solution. At the highest silane loading (7.2 wt %), the dense network restricts chain mobility, increasing stress while truncating extensibility and suppressing the J-curve. In contrast, the lowest loading (1.8 wt %) preserves high extensibility and creates a sparse covalent network that stabilizes the material without interfering with polymer-chain alignment. We therefore select 1.8 wt % as the optimum. Fourier-transform infrared spectroscopy (FTIR) verifies silane condensation (Figure 2D). The emergence of Si-O-Si (1,203 cm^{-1}) and Si-O-C (1,366 cm^{-1}) peaks confirms hydrolytic condensation of the silane functional groups grafted onto the PVA backbone. Complementary ^{1}H NMR characterization identifies the vinyl- and

Please cite this article in press as: Zhang et al., Replacing extraocular muscles with anisotropic, strain-stiffening hydrogels, Cell Biomaterials (2026), https://doi.org/10.1016/j.celbio.2026.100595

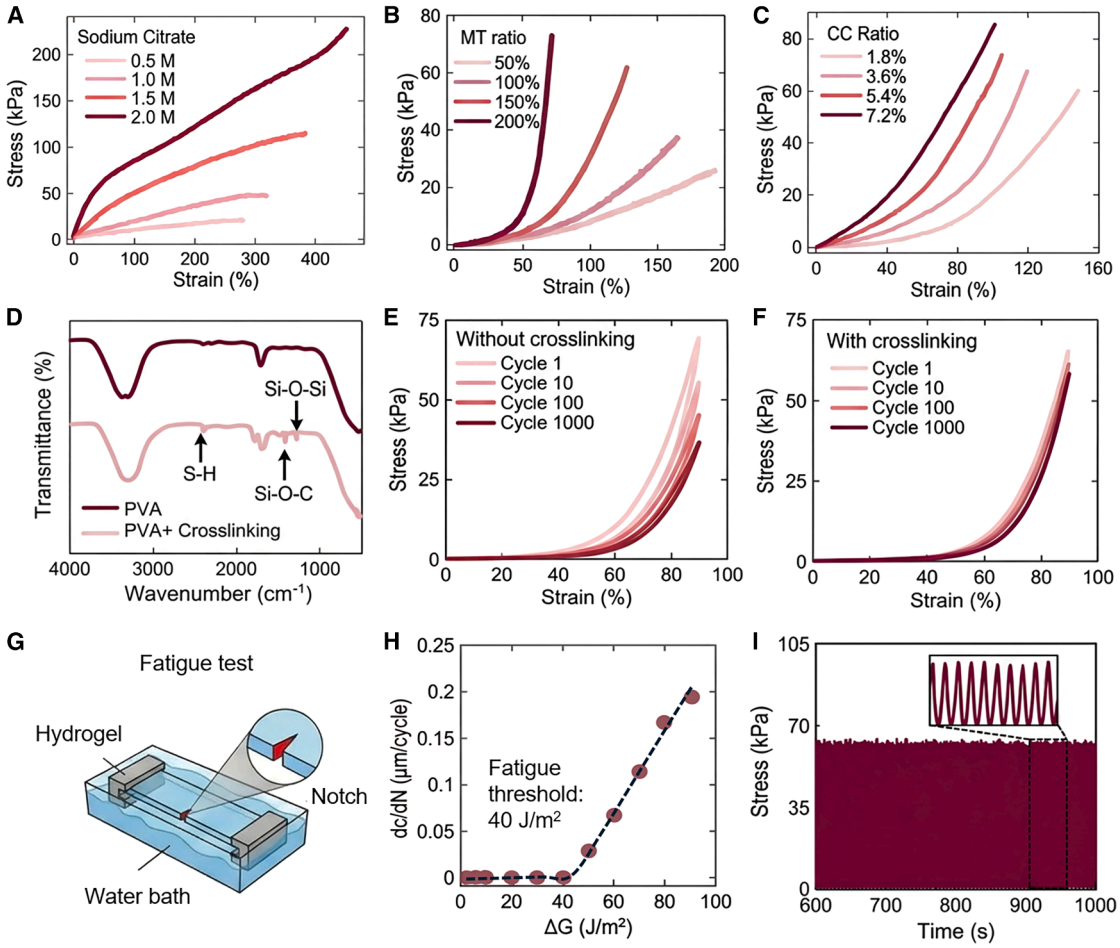

Figure 2. Engineering the J-curve and fatigue resistance

(A) Stiffness modulation by salting-out. Network densification with increasing citrate concentration.

(B) J-curve programming by mechanical training. Enhanced strain stiffening with increasing training ratio.

(C) Extensibility control by covalent crosslinking. Restriction of chain sliding by covalent bonds.

(D) Network formation by silane condensation. FTIR spectra showing Si-O-Si and Si-O-C peaks consistent with silane condensation.

(E and F) Cyclic stability from the covalent network. Cyclic softening of physically crosslinked hydrogels (E) and immediate stabilization of chemically crosslinked hydrogels (F).

(G–I) Fatigue characterization. Fracture-mechanics measurement of crack-growth resistance (G), determination of the fatigue threshold (H), and stable peak stress over 1,000 cycles (I).

mercaptopropyl-functionalized PVA precursors and shows attenuation of the vinyl resonances after UV exposure, consistent with thiol-ene conversion (Figure S8). Together, the silane condensation and thiol-ene reactions introduce sparse covalent network anchors. The physical crosslinks provide the nonlinear stiffness and energy dissipation, while the sparse covalent crosslinks act as permanent network anchors that prevent plastic deformation, enabling full recovery after thousands of loading cycles.

The implant is repeatedly loaded by eye movements. We therefore evaluate its mechanical stability under cyclic loading and resistance to crack growth. We subject the hydrogels to 1,000 cycles of loading at 100% strain. The response depends strictly on the network topology. A hydrogel with only physical crosslinks is unstable (Figure 2E). The peak stress decays progressively from 68–37 kPa. This softening occurs because the crystalline domains disrupt under load and cannot fully reform within the timescale of a cycle. The material effectively loses its initial network configuration. By contrast, the hydrogel with sparse chemical crosslinks (1.8 wt %) maintains stable peak stress over 1,000 cycles at 63 kPa (Figures 2F and 2I). The covalent bonds act as permanent network anchors; they maintain the network integrity while allowing the physical bonds to dynamically break and reform to dissipate energy. This architecture suppresses cyclic softening and stabilizes the peak stress under repeated loading (Figures 2F and 2I). We quantify the resistance to crack growth using fracture mechanics (Figure 2G). We measure the crack extension per cycle as a function of the energy release rate. The material exhibits a fatigue threshold of 40 J/m^2 (Figure 2H),[36] below which crack growth is suppressed under cyclic loading. This behavior supports resistance to fatigue-crack growth from microscopic flaws. Extended testing confirms

Please cite this article in press as: Zhang et al., Replacing extraocular muscles with anisotropic, strain-stiffening hydrogels, Cell Biomaterials (2026), https://doi.org/10.1016/j.celbio.2026.100595

CellPress
OPEN ACCESS

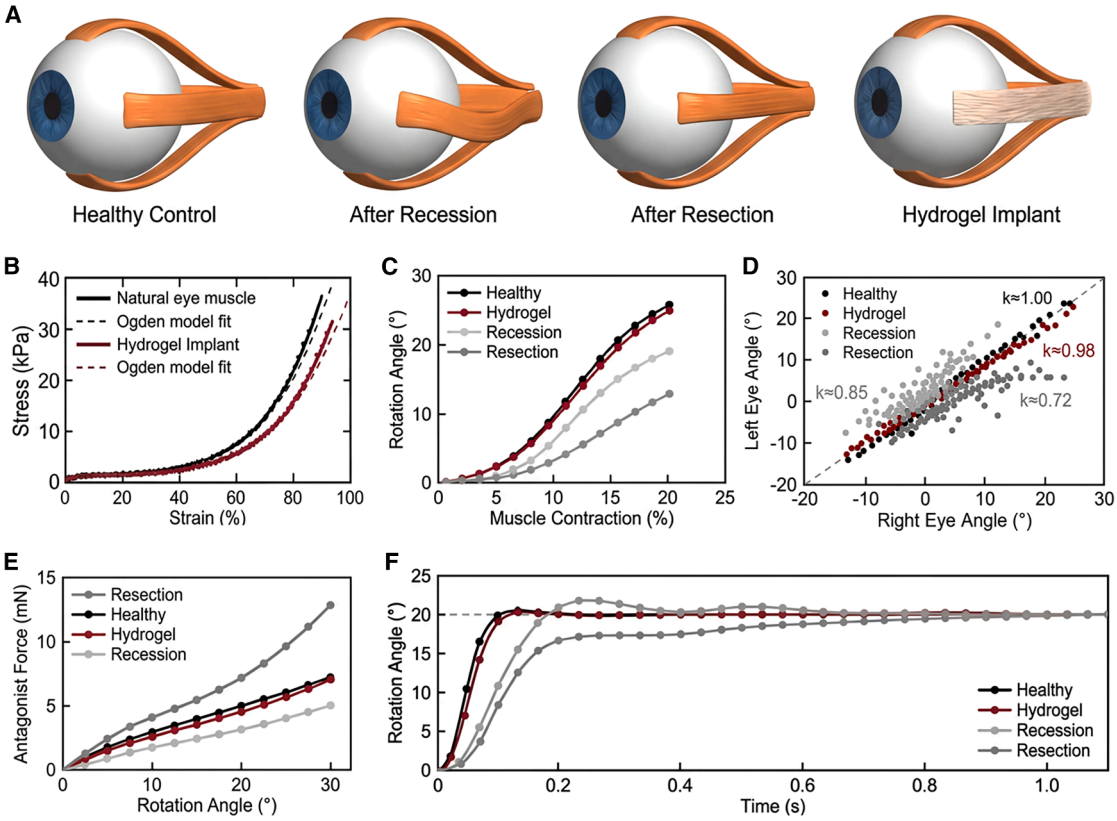

Figure 3. Simulation of functional restoration

(A) Finite element model configurations. Healthy, recessed, resected, and hydrogel-implanted states.
(B) Constitutive representation of muscle and hydrogel mechanics. Ogden-model fitting of the J-curves.
(C) Recovery of physiological rotation. Restoration of rotation angle by the hydrogel implant and deviation after recession or resection.
(D) Bilateral oculomotor coordination. Maintenance of left-right eye synchrony by the hydrogel implant.
(E) Passive-constraint mechanism. Resistance against antagonist-muscle loading and prevention of over-rotation by the implant.
(F) Saccade dynamics. Temporal matching between implanted and healthy eyes.

that the hydrogel sustains its mechanical profile over 10,000 cycles (Figure S5). Collectively, these results identify 1.5 M salting-out (for density), 150% mechanical training (for anisotropy), and 1.8 wt % chemical crosslinking (for stability) as the optimized processing condition for achieving a biomimetic J-curve with robust durability. This material is designed for operation in the dynamic orbital environment.

Simulation of eye dynamics

We simulate the eye-orbit system to validate that the material-level matching translates to system-level restoration. The three-dimensional model includes the globe and antagonistic rectus muscles (Figure 3A). We configure the lateral rectus in four states: healthy, recessed, resected, and implanted. The mechanical behaviors of the native muscle and the hydrogel are captured by a first-order Ogden hyperelastic model (Figure 3B; Table S1). This model reproduces the nonlinear stress-strain response within the strain range relevant to physiological eye rotation. We actuate the eye by contracting the medial rectus. The healthy eye rotates smoothly, reaching ~25° (Figure 3C). The hydrogel implant replicates this trajectory. The success relies on the J-curve: the compliant toe region permits initial rotation with minimal resistance, while the stiff heel region prevents over-rotation. By contrast, current surgeries fail to restore this balance. Recession creates slack, delaying force transmission and causing a lag in rotation. Resection pre-stretches the muscle, imposing continuous passive resistance that restricts the rotation to ~13°. This disparity is evident in bilateral oculomotor coordination (Figure 3D). We plot the rotation of the left eye against the right eye. The healthy control shows perfect synchrony. The hydrogel implant preserves this coordination. However, both recession and resection cause significant deviation. The simulation confirms that passive mechanical matching is necessary to restore complex oculomotor functions.

Dynamic vision imposes stringent requirements on kinetics. We quantify the force the antagonist muscle must exert to rotate the eye (Figure 3E). The hydrogel implant matches the force-angle relationship of the healthy control. The force remains low at small angles and rises nonlinearly to ~7 mN at 30°. This response derives strictly from the J-curve: the compliant toe region minimizes resistance to facilitate rotation, while the stiff heel region provides graded tension to stabilize the eye at large angles. By comparison, the surgical interventions disrupt this kinetics. Resection pre-stretches the muscle, doubling the

Please cite this article in press as: Zhang et al., Replacing extraocular muscles with anisotropic, strain-stiffening hydrogels, Cell Biomaterials (2026), https://doi.org/10.1016/j.celbio.2026.100595

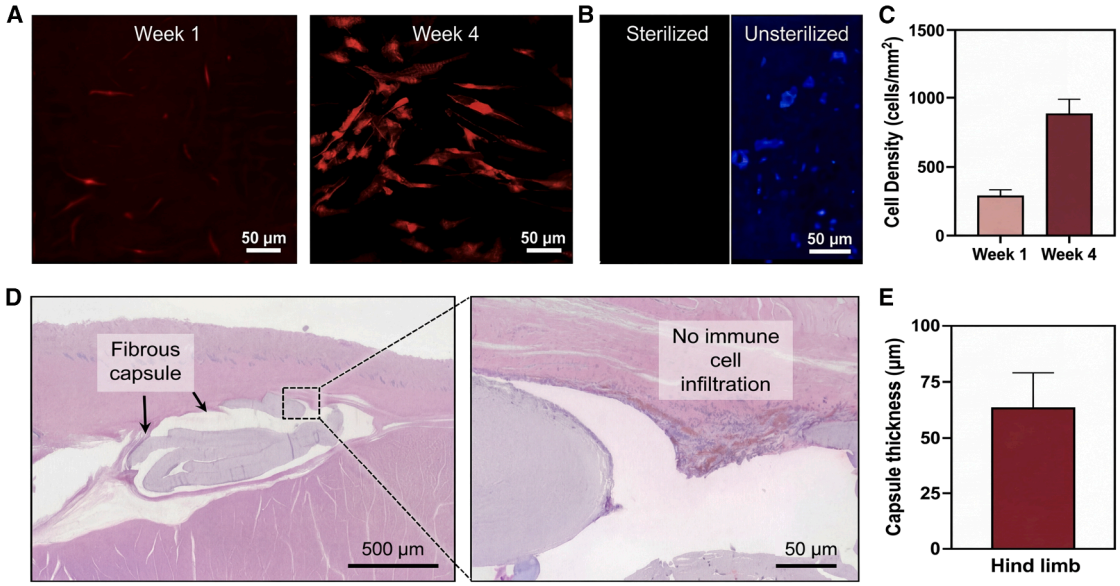

Figure 4. Biocompatibility and tissue integration

(A) Fibroblast culture. L929 fibroblasts attach and proliferate on the hydrogel over 4 weeks.

(B) Ethanol treatment. Ethanol-treated hydrogels remain free of bacterial contamination.

(C) Cell density. Quantification shows increased fibroblast density from weeks 1 to 4.

(D) Tissue integration. After subcutaneous implantation, the hydrogel remains intact with minimal inflammatory cell infiltration.

(E) Stable encapsulation. A thin fibrous capsule forms around the implant. Data are mean ± SD (C, E). Scale bars: 50 μm (A, B, D right); 500 μm (D left).

required force to ~13 mN. Recession introduces slack, requiring negligible force initially but failing to provide necessary tension for stability. We further simulate saccades by applying a step force (Figure 3F). The healthy eye reaches the 20° target in ~130 ms and stabilizes without oscillation. The hydrogel implant replicates this dynamic signature. The mechanism relies on the nonlinear stiffness: the low modulus at small strains enables rapid acceleration, whereas the high modulus at large strains prevents overshoot. Conversely, the recessed muscle leads to a time lag followed by significant overshoot due to the lack of passive constraint. The resected muscle leads to sluggish motion and fails to reach the target angle due to excessive resistance. The simulation confirms that reproducing the J-curve is a prerequisite for restoring physiological motor control.

Biocompatibility and integration

To assess the cytocompatibility of the thiol-ene crosslinked network, we culture L929 fibroblasts directly on the hydrogel surface (Figure 4A). The material supports cell viability and growth. At week 1, cells attach successfully. By week 4, they proliferate extensively and adopt the elongated, spindle-shaped morphology characteristic of healthy fibroblasts. Quantitative analysis reveals that the cell density triples from 297 to 892 cells/mm^2 (Figure 4C). This robust growth indicates no overt cytotoxicity under the tested conditions. We also confirm that routine ethanol treatment is compatible with the hydrogel before implantation (Figure 4B). Unsterilized samples show bacterial contamination, whereas ethanol-treated samples remain sterile without compromising cell attachment. These results establish that the engineered hydrogel combines the mechanical robustness required for function with the cytocompatibility required for integration.

We further evaluate the host response through subcutaneous implantation in a rabbit model. After 8 weeks, the harvested hydrogel remains structurally intact, without visible fragmentation or degradation. This stability arises from two complementary mechanisms. Dense hydrogen bonds within the crystalline domains immobilize the polymer chains, while sparse covalent crosslinks lock the network topology, together preventing further swelling beyond equilibrium. The interaction between the synthetic network and the biological tissue reaches a stable state. A thin fibrous capsule surrounds the implant. Histological analysis reveals that this capsule consists of organized collagen fibers and fibroblasts, free of immune cell infiltration. The mean capsule thickness is 64 μm (Figures 4D and 4E), indicating a mild foreign body reaction typical of biocompatible materials. We further evaluate local tolerance at the target application site. Hydrogels implanted at the lateral rectus position in the orbit elicit no overt inflammatory reaction (Figure S6). Despite its high vascularity and distinct immune privilege, the orbital environment tolerated the implant over the 8-week observation period. Together with benign fibrous encapsulation and intact implant morphology, these data support 8-week structural integrity and local tissue compatibility of the thiol-ene crosslinked hydrogel.

Functional restoration *in vivo*

We validate the functional restoration in a rabbit model. We compare three distinct mechanical states: the intact eye, the muscle-removed eye, and the implanted eye. In the implanted group, we suture the hydrogel between the sclera and the orbital

Please cite this article in press as: Zhang et al., Replacing extraocular muscles with anisotropic, strain-stiffening hydrogels, Cell Biomaterials (2026), https://doi.org/10.1016/j.celbio.2026.100595

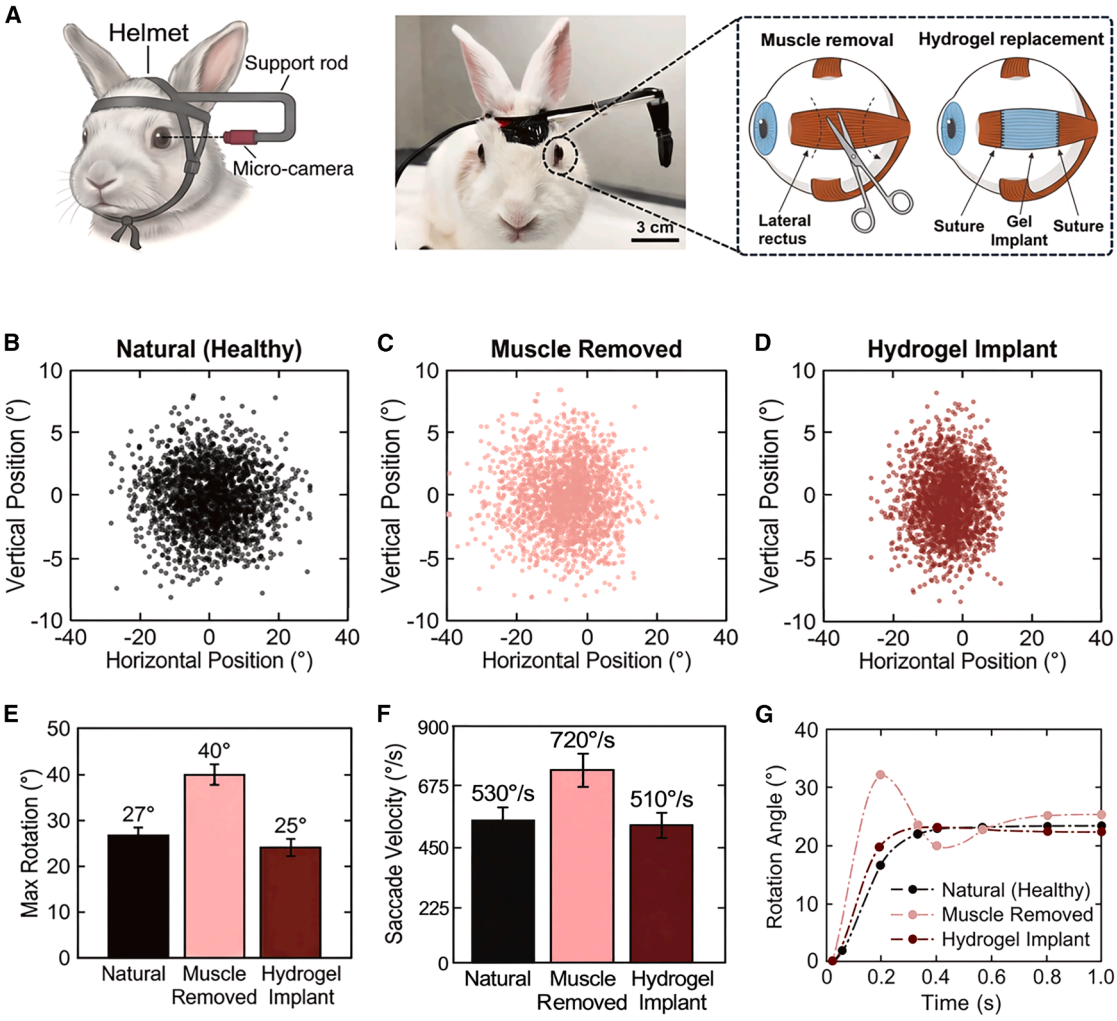

Figure 5. Restoration of function *in vivo*

(A) Eye-tracking setup. Head-mounted camera recording of rabbit eye movement after hydrogel implantation.

(B–D) Passive-constraint mechanism. Physiological rotation of the healthy eye (B), pathological over-rotation after lateral rectus removal (C), and over-rotation suppression by the hydrogel implant (D).

(E) Range-of-motion recovery. Restoration of functional rotation with prevention of over-rotation.

(F) Saccade-velocity recovery. Rapid acceleration of the implanted eye (~510°/s).

(G) Optokinetic gaze stabilization. Stable target tracking by the implanted eye without oscillation. Data are mean ± SD (E, F). Scale bar: 3 cm (A).

wall to replace the excised lateral rectus (Figures 5A and S7). We quantify the eye movement dynamics using a head-mounted camera. The intact eye operates within a stable physiological window. The gaze distribution is symmetric and strictly confined within a range of ±27° (Figure 5B). The native muscle acts as a check ligament. Removing the muscle eliminates this constraint. The eye loses stability. The gaze distribution becomes erratic and highly biased, with frequent pathological excursions exceeding 40° (Figure 5C). This "overshoot" signifies the complete loss of passive tension. The hydrogel implant restores the constraint. Although the distribution remains asymmetric due to the lack of active contraction, the implant effectively eliminates the pathological overshoot (Figure 5D; Video S1). The eye is once again confined within the physiological limit. This restoration derives directly from the J-curve: the hydrogel remains compliant during normal gaze to allow movement but stiffens sharply at large angles to halt the rotation. The experiment demonstrates that a passive material, when engineered with the correct nonlinearity, is sufficient to stabilize the oculomotor system against pathological drift.

We quantify the functional restoration using three metrics. First, we measure the range of motion (Figure 5E). The natural eye is constrained to a rotation of 27°, consistent with the physiological saccade amplitude range reported for rabbits (mean 20.6° ± 12.4°).[37] Removal of the lateral rectus abolishes this constraint, resulting in pathological hypermobility with a rotation of 40°, well outside this physiological range. The hydrogel implant re-establishes the limit, restricting the rotation to 25°, statistically indistinguishable from the intact eye and within the physiological saccade window. This restoration represents

Please cite this article in press as: Zhang et al., Replacing extraocular muscles with anisotropic, strain-stiffening hydrogels, Cell Biomaterials (2026), https://doi.org/10.1016/j.celbio.2026.100595

biomechanical normalization rather than overcorrection. This confirms that the implant provides the necessary passive tension at large strains to prevent over-rotation. Second, we analyze the saccade velocity (Figure 5F). The dynamic balance of the eye depends on the antagonism between the active agonist and the passive antagonist. Without the lateral rectus, the eye accelerates excessively to 720°/s. The implant restores the antagonistic resistance, normalizing the velocity to 510°/s, close to the natural speed of 530°/s. Third, we evaluate optokinetic gaze stabilization (Figure 5G). Stability is compromised in the muscle-removed eye, which exhibits oscillations and overshoots. The implanted eye tracks the moving target stably. These results validate the design principle. The hydrogel does not merely fill space; it functions mechanically. By recapitulating the J-curve, the implant restores the passive constraint essential for normalizing the rotation range, dynamics, and stability.

DISCUSSION

Restoring oculomotor dynamics requires more than static realignment; it requires matching the passive mechanics of the native tissue. The extraocular muscle functions as a nonlinear spring, compliant at small strains to permit rapid saccades but stiffening sharply at large strains to act as a check ligament.[38] We replicate this J-shaped stress-strain behavior in a synthetic hydrogel through a hierarchy of freezing, salting-out, training, and crosslinking. This approach addresses a fundamental limitation of current surgeries: recession introduces slack that delays force transmission, while resection introduces pre-stretch that imposes excessive drag. Neither procedure can restore tension to a paralyzed or fibrotic muscle that has lost contractility, and the eye loses passive stability. Our hydrogel implant restores this passive constraint by providing low resistance within the physiological range and high resistance at the rotational limit, thereby recovering the dynamic equilibrium of the eye.[39]

This passive mechanical replacement extends therapeutic options to conditions where the muscle is no longer mechanically functional. Patients with paralytic strabismus or congenital fibrosis lack the contractility required for recession or resection, leaving the eye without the passive elastic constraint that limits over-rotation. By restoring this constraint with a synthetic implant rather than acting on residual muscle, our approach operationalizes a design principle: matching the nonlinear passive response of a tissue can substitute for its lost passive function, independent of active force generation.

Three practical limitations remain before clinical translation. (1) Differences between rabbit and human orbital anatomy and extraocular muscle mechanics require validation in primate models. (2) The 8-week observation captures the early host response but not chronic remodeling, chronic immune response, sustained mechanical fidelity, or comprehensive ophthalmological assessment, including intraocular pressure, fundoscopy, and refraction. (3) Total fabrication requires ~1 week, dominated by salting-out (up to 4 days) and mechanical training; accelerated salting-out kinetics and optimized solution exchange are practical process-improvement strategies. Beyond these, the implant is purely passive: it functions as a nonlinear spring that prevents instability but does not generate active force. Full restoration of dynamic gaze requires integration of active actuation, for which electroactive and stimuli-responsive mechanisms are under exploration.[40–42] This work demonstrates that treating mechanical deficiency requires matching the full nonlinear stress-strain response of native tissue, not a single modulus.[43] The same principle applies to nonlinearly compliant soft tissues including tendons, ligaments, and cardiac muscles.[44,45] The combination of hierarchical structure, nonlinear mechanics, and covalent crosslinking provides a general framework for engineering passive mechanical replacements of these tissues.

METHODS

Materials

PVA (Mw 89,000, 99+% hydrolyzed) and sodium citrate tribasic dihydrate were purchased from Sigma-Aldrich. MPTES (Sigma-Aldrich, ≥95%) was used to introduce pendant thiol groups onto PVA chains. VDMES (Gelest, ≥97%) was used to introduce vinyl functionalities. 2-hydroxy-4′-(2-hydroxyethoxy)-2-methylpropiophenone (Irgacure 2959, BASF) served as the UV photoinitiator. All chemicals were used as received without further purification.

Hydrogel fabrication

PVA solution (10 wt %) was prepared by dissolving PVA powder in deionized water under vigorous stirring and heating (70°C). After degassing by sonication for 1 h, a clear solution was obtained. A 1.5 M sodium citrate solution was prepared by dissolving sodium citrate tribasic dihydrate in deionized water, followed by sonication for 10 min. An ethanol bath at −80°C was used as the immersion bath for ice-templating, with temperature maintained using an EYELA-PSL1810 constant-temperature bath. The PVA aqueous precursor was poured into an acrylic container with peripheral thermal insulation and a glass bottom for good thermal conduction. The container was lowered into the ethanol bath at an immersion rate of 1 mm min^{-1}. The directionally frozen PVA solution was then immersed into 1.5 M sodium citrate solution for gelation for up to 4 days.[26] For chemical crosslinking, two functionalized PVA precursor solutions were prepared in parallel using a stoichiometric thiol:vinyl feed. The total silane loading was defined as the combined mass of MPTES and VDMES relative to the mass of the 10 wt % PVA precursor solution. For a 10 g batch of 10 wt % PVA precursor at the optimized 1.8 wt % total silane loading, the feed contained 0.116 g MPTES and 0.064 g VDMES. This composition corresponds to 0.488 mmol MPTES-derived thiol groups and 0.488 mmol VDMES-derived vinyl groups per gram of total PVA, equivalent to a nominal average density of 2.15 mol% for each complementary reactive group per PVA repeat unit (4.30 mol % total pendant reactive groups). Other silane loadings were calculated using the same stoichiometric MPTES/VDMES ratio. In the first solution, MPTES and Irgacure 2,959 (0.012 g per 10 g of 10 wt % PVA solution) were added to PVA (10 wt % in deionized water) and stirred for 15 min. The pH was adjusted to 5–6 with 0.1 M acetic acid and the solution was stirred for an additional 45 min to allow silane hydrolysis and condensation with the PVA hydroxyls.[46,47] In the second solution, VDMES was added to PVA (10 wt % in deionized water) and stirred for 15 min, followed by pH

Please cite this article in press as: Zhang et al., Replacing extraocular muscles with anisotropic, strain-stiffening hydrogels, Cell Biomaterials (2026), https://doi.org/10.1016/j.celbio.2026.100595

adjustment to 5–6 with 0.1 M acetic acid and stirring for 45 min. The two functionalized PVA solutions were combined at equal volumes and homogenized using a planetary centrifugal mixer. After mechanical training (50 cycles of uniaxial stretching to 150% strain), the precursor-loaded hydrogel was irradiated under a 365 nm UV lamp for 2 h to initiate thiol-ene click reactions between thiol- and vinyl-functionalized PVA chains.[47] ^{1}H NMR spectra were collected to evaluate silane functionalization and thiol-ene conversion (Figure S8).

Scanning electron microscopy

For characterization of the structure of the hierarchically aligned hydrogels, all hydrogel samples were immersed in deionized water for 24 h to reach equilibrium before freeze-drying using a Labconco FreeZone freeze-dryer. The freeze-dried hydrogels were cryogenically fractured in liquid nitrogen along the aligned direction to expose their interior and sputter-coated with gold before imaging at 10 kV using a FEI Teneo scanning electron microscope.

FTIR

FTIR spectra were recorded at room temperature using an attenuated total reflectance mode (ATR-FTIR, Nicolet Summit X, Thermo Scientific). Each spectrum was averaged from 10 scans over the range of 4,000–400 cm^{-1}. ^{1}H NMR spectra were acquired on a 400 MHz Bruker spectrometer; chemical shifts are reported in ppm.

SAXS

2D SAXS measurements were performed at beamline 12-ID-B of the advanced photon source (Argonne National Laboratory). Hydrated PVA hydrogel samples were measured at room temperature in water. SAXS patterns were collected using an Eiger 9M detector at an X-ray energy of 13.3 keV (wavelength, 0.932 Å), a sample-to-detector distance of approximately 1.99 m, and an exposure time of 0.2 s, covering a q range of 0–0.876 $Å^{-1}$. Multiple positions were measured for each hydrated sample. Frames containing bubbles, sample-edge artifacts, beamstop shadow, or detector artifacts were masked or excluded before azimuthal averaging. Azimuthal intensity profiles were obtained from the corrected 2D SAXS patterns by pyFAI caking over q = 0.010-0.020 $Å^{-1}$ and plotted as normalized intensity versus azimuthal angle.

For equilibrium water content measurements, hydrogel samples were equilibrated in deionized water for 24 h. Excess surface water was gently removed before measuring the hydrated mass (m_w). The samples were then freeze-dried to obtain the dry mass (m_d), and water content was calculated as $[(m_w - m_d)/m_w] \times 100\%$. Error bars represent standard deviations from replicate specimens.

Mechanical testing

The hydrogels were cut into dogbone-shaped specimens with a gauge width of 5 mm, gauge length of 10 mm, and thickness of 0.8 mm. The force-displacement data were obtained using a Cellscale Univert mechanical tester equipped with 50 and 200 N load cells. The stress-strain curves were obtained by dividing the measured force by the initial gauge cross-section area and the measured displacement by the initial clamp distance. Five hydrogel specimens were tested for each condition, and the specimens were loaded at a strain rate of 10% s^{-1}.[25] A single freshly-excised rabbit lateral rectus muscle was tested under the same uniaxial protocol within 1 h of explantation to obtain the native extraocular muscle (EOM) stress-strain response (Figures 1E and 3B).[27]

For short-term cyclic loading tests, samples were subjected to 1,000 loading-unloading cycles at 100% strain (1 Hz) to evaluate stress decay (Figures 2E, 2F, and 2I). To examine long-term durability, extended cyclic loading was performed for 10,000 cycles at 100% strain (1 Hz) on the optimized formulation, with peak stress recorded throughout (Figure S5).

Fatigue testing was performed in a water bath to prevent dehydration. Cyclic tensile tests were conducted using notched samples with an initial crack length smaller than one-fifth of the sample width. The energy release rate (G) was calculated as

$$G = 2k(\lambda)cW(\lambda, N)$$

where $k(\lambda) = \frac{3}{\sqrt{\lambda}}$ is the slowly varying geometric factor, λ is the applied stretch, c is the current crack length, and W(λ, N) is the strain energy density of an unnotched sample at the Nth cycle of applied stretch λ.[48,49] The fatigue threshold Γ_0 was determined as the intercept of the linear extrapolation of $\frac{dc}{dN}$ versus G with the abscissa.[27,48,49]

Finite element simulation

Three-dimensional finite element models of the rabbit eye-orbit system were constructed in COMSOL Multiphysics 6.1. The model comprised a globe (approximated as a sphere with 18 mm equatorial diameter; rabbit globe axial length is ~16.6 mm; the spherical approximation introduces less than 2% error in rotation angle predictions) and two pairs of antagonistic rectus muscles. The natural extraocular muscle and the hydrogel implant were modeled with a first-order Ogden hyperelastic constitutive law:[50]

$$\sigma(\lambda) = \left(\frac{2\mu}{\alpha}\right)\left(\lambda^{\alpha} - \lambda^{-\frac{\alpha}{2}}\right)$$

Parameters μ and α were fitted to uniaxial tensile data using an inverse finite element approach. For the native rabbit lateral rectus muscle, $\mu = 2.5$ kPa and $\alpha = 10$ ($R^2 = 0.97$); for the hydrogel implant, $\mu = 3.0$ kPa and $\alpha = 9$ ($R^2 = 0.98$), spanning the strain range 0%–50% relevant to physiological eye rotation (Table S1). Muscle activation was simulated by applying a contractile strain to the medial rectus while monitoring the rotation angle of the globe. Mesh convergence was verified by ensuring less than 2% variation in predicted rotation angles upon refinement.

Cell culture and cytocompatibility assessment

L929 cells were purchased from the American Type Culture Collection (ATCC) and cultured in Dulbecco's modified Eagle's medium (DMEM) (Gibco). Cells were cultured at 37°C with 5% CO_2 in an incubator.[51] Cell culture medium was supplemented with 10% (v/v) fetal bovine serum (Gibco) and

Please cite this article in press as: Zhang et al., Replacing extraocular muscles with anisotropic, strain-stiffening hydrogels, Cell Biomaterials (2026), https://doi.org/10.1016/j.celbio.2026.100595

penicillin/streptomycin (100 U/ml; Invitrogen). Hydrogel samples were sterilized with ethanol and equilibrated in culture medium for 24 h before cell seeding. Cells were seeded onto hydrogel surfaces at a density of 1×10^4 cells/cm^2 and cultured for up to 4 weeks. Cell morphology was visualized by fluorescence microscopy (Zeiss Axio Observer). Cell density was quantified by counting cells in five randomly selected fields per sample.

In vivo animal model and ethical approval

All animal procedures were approved by the Institutional Animal Care and Use Committee/Animal Research Committee at the University of California, Los Angeles (UCLA ARC Protocol# ARC-2021-084) in compliance with Animal Research: Reporting In Vivo Experiments (ARRIVE) guidelines and the NIH Guide. Adult New Zealand White rabbits (Oryctolagus cuniculus, strain Crl:KBL(NZW), body weight 2.5–3.1 kg, specific pathogen-free (SPF); Charles River Laboratories) were housed in the UCLA CHS Vivarium under standard conditions (20°C–22°C, 30%–70% humidity, 12 h light/dark cycle) with *ad libitum* food and water. Animals underwent acclimatization (≥10 days) prior to procedures. This pilot feasibility study utilized $n = 3$ rabbits for sequential within-subject longitudinal tracking (intact baseline, muscle extirpation defect, and hydrogel implantation) to validate functional restoration while adhering to 3R principles. The individual rabbit was the experimental unit. Animals were not randomly allocated to separate groups because each rabbit underwent the same prespecified, irreversible sequence of intact baseline, lateral rectus muscle extirpation, and hydrogel implantation; accordingly, no allocation sequence was generated and allocation concealment was not applicable. Treatment order was fixed by design. Cage positions changed periodically as part of routine vivarium husbandry and were not systematically assigned according to experimental condition.

Lateral rectus muscle extirpation

After adequate anesthesia was obtained, a conjunctival peritomy was created at the temporal limbus. Relaxing incisions were made to allow access to the posterior lateral rectus. The lateral rectus muscle was isolated on a muscle hook. Careful dissection was performed to ensure that the entire lateral rectus could be visualized. Electrocautery was applied to minimize bleeding, and the lateral rectus was extirpated as far back as possible. Approximately 14 mm of the muscle was removed. After that, the conjunctiva was closed using absorbable sutures and the rabbit was allowed to recover for 4 weeks before the next procedure.

Hydrogel implantation

After adequate anesthesia was obtained, forced duction testing was performed to ensure that there was no restriction from the prior surgery. No restriction was found in any case. The original conjunctival peritomy was reopened using surgical scissors. Relaxing incisions were again fashioned. The area where the prior extirpation was inspected and no remaining muscle fibers could be found. Straight scissors were used to dissect down to the lateral orbital rim of the rabbit. Once the lateral orbital rim could be visualized, a 5-0 Mersilene suture was passed through the orbital periosteum. The same suture was then passed through one end of the hydrogel. The hydrogel was trimmed such that it was long enough to be sutured to the original lateral rectus muscle insertion with the eye straight ahead in primary position. Using this length of the hydrogel, a second suture was passed through the other end of the hydrogel and that same suture was used to suture the hydrogel to the original lateral rectus muscle insertion. The sutures were trimmed, and the conjunctiva was closed using absorbable sutures.

Eye movement tracking

Eye movements were recorded at 4 weeks post-surgery using a custom head-mounted micro-camera system. The system comprised a lightweight helmet secured to the rabbit's head and a micro-camera (30 fps) positioned to capture the eye. Pupil position was extracted using automated tracking algorithms implemented in MATLAB. Rotation angles were calculated using a calibrated geometric model relating pupil displacement to eye rotation. Recording sessions lasted 5 min during free-viewing behavior in an illuminated arena. Maximum rotation angles and saccade velocities were extracted from the recorded trajectories. Investigators performing the surgical procedures and video acquisition were aware of the experimental condition because of the sequential design. Before tracking, video files were coded and their analysis order was randomized by an investigator who did not participate in tracking or final statistical analysis. Experimental-condition labels were concealed from personnel performing outcome assessment and statistical analysis until analyses were completed.

Histological analysis

Animals were euthanized at 8 weeks post-implantation, and implant sites (hind limbs and head) were harvested for histological evaluation. Tissues were fixed in 10% neutral buffered formalin. The head was decalcified in a solution of 50% formic acid and 50% sodium citrate prior to sectioning. Tissues were trimmed, paraffin-embedded, sectioned at 5 μm thickness, and stained with hematoxylin and eosin (H&E). Histopathological evaluation was performed by a board-certified veterinary pathologist (Diplomate ACVP) at IDEXX BioAnalytics who was blinded to experimental groups. Microscopic changes were graded utilizing the International Harmonization of Nomenclature and Diagnostic (INHAND) criteria standards. Fibrous capsule thickness was measured at five locations per sample.[52]

Statistical analysis

Data are presented as mean ± SD (or mean ± SEM where indicated). Statistical analyses were performed using MATLAB 2023b. Normality of data distribution was confirmed using the Shapiro-Wilk test. Comparisons between two groups were analyzed using paired or unpaired two-tailed Student's *t* tests. Comparisons among three conditions (intact, extirpated, and implanted) were conducted using one-way repeated-measures ANOVA followed by Tukey's post hoc multiple comparisons. Differences were considered statistically significant at $p < 0.05$.

RESOURCE AVAILABILITY

Lead contact

Requests for further information, resources, and reagents should be directed to and will be fulfilled by the lead contact, Prof. Ximin He (ximinhe@ucla.edu).

Materials availability

No novel and distinctive reagents were produced in this study.

Data and code availability

All data supporting the findings of this study are available within this paper and the supplemental information. Any additional information required to reanalyze the data reported in this paper is available from the lead contact upon request.

ACKNOWLEDGMENTS

This work was supported by the award for Research to Prevent Blindness Unrestricted and Innovation Funds (S.L.P. and F.G.V.), NIH award R01DK132319, the Office of Naval Research (ONR) awards (N000142412187 and N000142212595), and the Moore Foundation Award (12072). This research was performed on APS beam time award (https://doi.org/10.46936/APS-194385/60017047) from the Advanced Photon Source, a US Department of Energy (DOE) Office of Science user facility operated for the DOE Office of Science by Argonne National Laboratory under contract no. DE-AC02-06CH11357.

AUTHOR CONTRIBUTIONS

Conceptualization, X.H., F.G.V., S.L.P., and C.W.Z.; methodology, C.W.Z., Y.D., R.K., H.Z., Y.Z., F.G.V., and S.L.P.; investigation, C.W.Z., Y.D., R.K., W.H., Z.L., D.Y., and M.P.; finite element simulation, C.W.Z. and Z.L.; surgical procedures, F.G.V. and S.L.P.; writing – original draft, C.W.Z., Y.D., R.K., and X.H.; writing – review and editing, C.W.Z., Y.D., R.K., W.H., Z.L., D.Y., C.C., H.Z., Y.Z., F.G.V., S.L.P., and X.H.; supervision, X.H., F.G.V., and S.L.P.; and funding acquisition, X.H., F.G.V., and S.L.P.

DECLARATION OF INTERESTS

The authors declare no competing interests.

SUPPLEMENTAL INFORMATION

Supplemental information can be found online at https://doi.org/10.1016/j.celbio.2026.100595.

Received: December 31, 2025
Revised: July 9, 2026
Accepted: August 24, 2026

REFERENCES

1. Velez, F.G., Velez, G., Hendler, K., and Pineles, S.L. (2012). Isolated y-splitting and recession of the lateral rectus muscle in patients with exo-duane syndrome. Strabismus *20*, 109–114. https://doi.org/10.3109/09273972.2012.702323.
2. Pineles, S.L., Chang, M.Y., and Velez, F.G. (2020). Compartmental Strabismus. J. Binocul. Vis. Ocul. Motil. *70*, 71–78. https://doi.org/10.1080/2576117x.2020.1760683.
3. Chang, M.Y., Demer, J.L., Isenberg, S.J., Velez, F.G., and Pineles, S.L. (2017). Decreased Binocular Summation in Strabismic Amblyopes and Effect of Strabismus Surgery. Strabismus *25*, 73–80. https://doi.org/10.1080/09273972.2017.1318153.
4. Arblaster, G.E., Davis, H., Buckley, D., and Barnes, S. (2024). Patient perspectives on their outcomes from strabismus surgery undertaken for psychosocial reasons. Eye (Lond.) *38*, 2926–2931. https://doi.org/10.1038/s41433-024-03189-9.
5. Pineles, S.L., Chang, M.Y., Holmes, J.M., Kekunnaya, R., Özkan, S.B., and Velez, F.G. (2019). Innovative techniques for the treatment of adult strabismus. J. AAPOS *23*, 132–139. https://doi.org/10.1016/j.jaapos.2018.10.018.
6. Peragallo, J.H., Velez, F.G., Demer, J.L., and Pineles, S.L. (2013). Long-term follow-up of strabismus surgery for patients with ocular myasthenia gravis. J. Neuroophthalmol. *33*, 40–44. https://doi.org/10.1097/WNO.0b013e318280d630.
7. Sunyer-Grau, B., Quevedo, L., Rodríguez-Vallejo, M., and Argilés, M. (2023). Comitant strabismus etiology: extraocular muscle integrity and central nervous system involvement-a narrative review. Graefes Arch. Clin. Exp. Ophthalmol. *261*, 1781–1792. https://doi.org/10.1007/s00417-022-05935-9.
8. Zhou, T., Guo, W., Zhu, X., Jing, Y., Shao, Q., Shen, S., Chen, X., Leng, Z., Liu, B., Zhang, S., et al. (2025). Comparison of Two Different Extraocular Muscle Suturing Techniques for Strabismus Surgery. Am. J. Ophthalmol. *278*, 131–139. https://doi.org/10.1016/j.ajo.2025.06.019.
9. Yang, S.A., Choi, H.Y., Kim, S.J., Han, K.E., and Lee, J.E. (2024). Factors Associated with Surgical Outcomes after Bilateral Lateral Rectus Recession in Children with Intermittent Exotropia. J. Clin. Med. *13*, 731. https://doi.org/10.3390/jcm13030731.
10. Leffler, C.T., Varrone, E., Paruchuri, S.S., and Phan, C. (2026). The Optimal Surgical Strategy and Dose for Esotropia. Cureus *18* (9), e115667. https://doi.org/10.7759/cureus.115667.
11. Behbehani, R. (2023). Ocular Myasthenia Gravis: A Current Overview. Eye Brain *15*, 1–13. https://doi.org/10.2147/eb.S389629.
12. Xia, W., Wei, Y., Wu, L., and Zhao, C. (2022). Congenital Fibrosis of the Extraocular Muscles: An Overview from Genetics to Management. Children (Basel) *9*, 1605. https://doi.org/10.3390/children9111605.
13. Evoli, A., and Iorio, R. (2020). Controversies in Ocular Myasthenia Gravis. Front. Neurol. *11*, 605902. https://doi.org/10.3389/fneur.2020.605902.
14. Wang, Y.J., Zhang, X.N., Song, Y., Zhao, Y., Chen, L., Su, F., Li, L., Wu, Z.L., and Zheng, Q. (2019). Ultrastiff and Tough Supramolecular Hydrogels with a Dense and Robust Hydrogen Bond Network. Chem. Mater. *31*, 1430–1440. https://doi.org/10.1021/acs.chemmater.8b05262.
15. Arif, M., Zhang, J., Xu, R., Yu, C., Majid, M., Guimarães, C.F., Li, G., Yu, T., Zhou, Q., and Reis, R.L. (2025). Soft Bio-Electroactive Hydrogels for Musculoskeletal Tissue Repair and Rehabilitation. Adv. Healthc. Mater. *14*, e2502497. https://doi.org/10.1002/adhm.202502497.
16. Hong, L.T.A., Kim, Y.M., Park, H.H., Hwang, D.H., Cui, Y., Lee, E.M., Yahn, S., Lee, J.K., Song, S.C., and Kim, B.G. (2017). An injectable hydrogel enhances tissue repair after spinal cord injury by promoting extracellular matrix remodeling. Nat. Commun. *8*, 533. https://doi.org/10.1038/s41467-017-00583-8.
17. Chavan, R., Kamble, N., Kuthe, C., and Sarnobat, S. (2024). On Mechanical Behavior and Characterization of Soft Tissues. Biomed. Eng. Comput. Biol. *15*, 11795972241294115. https://doi.org/10.1177/11795972241294115.
18. Mladenovic, T., Zivic, F., Petrovic, N., Njezic, S., Pavic, J., Kotorcevic, N., Milenkovic, S., and Grujovic, N. (2024). Application of Silicone in Ophthalmology: A Review. Materials (Basel) *17*, 3454. https://doi.org/10.3390/ma17143454.
19. Valentín-Bravo, F.J., García-Onrubia, L., Andrés-Iglesias, C., Valentín-Bravo, E., Martín-Vallejo, J., Pastor, J.C., Usategui-Martín, R., and Pastor-Idoate, S. (2022). Complications associated with the use of silicone oil in vitreoretinal surgery: A systemic review and meta-analysis. Acta Ophthalmol. *100*, e864–e880. https://doi.org/10.1111/aos.15055.
20. Jaklová, N., and Kamenická, B. (2026). In vitro silicone oil emulsification in retinal detachment treatment: Methods, designs, and future strategies. Acta Biomater. *210*, 413–440. https://doi.org/10.1016/j.actbio.2025.12.024.
21. Vatankhah-Varnosfaderani, M., Daniel, W.F.M., Everhart, M.H., Pandya, A.A., Liang, H., Matyjaszewski, K., Dobrynin, A.V., and Sheiko, S.S.

(2017). Mimicking biological stress–strain behaviour with synthetic elastomers. Nature *549*, 497–501. https://doi.org/10.1038/nature23673.

22. Zhao, X., Chen, X., Yuk, H., Lin, S., Liu, X., and Parada, G. (2021). Soft Materials by Design: Unconventional Polymer Networks Give Extreme Properties. Chem. Rev. *121*, 4309–4372. https://doi.org/10.1021/acs.chemrev.0c01088.
23. Ma, Y., Hua, M., Wu, S., Du, Y., Pei, X., Zhu, X., Zhou, F., and He, X. (2020). Bioinspired high-power-density strong contractile hydrogel by programmable elastic recoil. Sci. Adv. *6*, eabd2520. https://doi.org/10.1126/sciadv.abd2520.
24. Gong, J.P. (2010). Why are double network hydrogels so tough? Soft Matter *6*, 2583–2590. https://doi.org/10.1039/B924290B.
25. Zhao, X. (2017). Designing toughness and strength for soft materials. Proc. Natl. Acad. Sci. USA *114*, 8138–8140. https://doi.org/10.1073/pnas.1710942114.
26. Wu, S., Hua, M., Alsaid, Y., Du, Y., Ma, Y., Zhao, Y., Lo, C.-Y., Wang, C., Wu, D., Yao, B., et al. (2021). Poly(vinyl alcohol) Hydrogels with Broad-Range Tunable Mechanical Properties via the Hofmeister Effect. Adv. Mater. *33*, e2007829. https://doi.org/10.1002/adma.202007829.
27. Hua, M., Wu, S., Ma, Y., Zhao, Y., Chen, Z., Frenkel, I., Strzalka, J., Zhou, H., Zhu, X., and He, X. (2021). Strong tough hydrogels via the synergy of freeze-casting and salting out. Nature *590*, 594–599. https://doi.org/10.1038/s41586-021-03212-z.
28. Zhang, X.N., Wang, Y.J., Sun, S., Hou, L., Wu, P., Wu, Z.L., and Zheng, Q. (2018). A Tough and Stiff Hydrogel with Tunable Water Content and Mechanical Properties Based on the Synergistic Effect of Hydrogen Bonding and Hydrophobic Interaction. Macromolecules *51*, 8136–8146. https://doi.org/10.1021/acs.macromol.8b01496.
29. Zhu, S., Wang, S., Huang, Y., Tang, Q., Fu, T., Su, R., Fan, C., Xia, S., Lee, P.S., and Lin, Y. (2024). Bioinspired structural hydrogels with highly ordered hierarchical orientations by flow-induced alignment of nanofibrils. Nat. Commun. *15*, 118. https://doi.org/10.1038/s41467-023-44481-8.
30. Li, H., Wu, H., Guan, C., Hu, W., Su, W., Chen, D., and Gao, J. (2025). Hierarchical crack-resistant, tissue-mimetic hydrogels enabled by progressive nanocrystallization of anisotropic polymer networks. Nat. Commun. *16*, 10890. https://doi.org/10.1038/s41467-025-65917-3.
31. Lin, S., Liu, J., Liu, X., and Zhao, X. (2019). Muscle-like fatigue-resistant hydrogels by mechanical training. Proc. Natl. Acad. Sci. USA *116*, 10244–10249. https://doi.org/10.1073/pnas.1903019116.
32. Zhao, X. (2014). Multi-scale multi-mechanism design of tough hydrogels: building dissipation into stretchy networks. Soft Matter *10*, 672–687. https://doi.org/10.1039/C3SM52272E.
33. Zhang, G., Steck, J., Kim, J., Ahn, C.H., and Suo, Z. (2023). Hydrogels of arrested phase separation simultaneously achieve high strength and low hysteresis. Sci. Adv. *9*, eadh7742. https://doi.org/10.1126/sciadv.adh7742.
34. Yuk, H., Varela, C.E., Nabzdyk, C.S., Mao, X., Padera, R.F., Roche, E.T., and Zhao, X. (2019). Dry double-sided tape for adhesion of wet tissues and devices. Nature *575*, 169–174. https://doi.org/10.1038/s41586-019-1710-5.
35. Sun, X., Mao, Y., Yu, Z., Yang, P., and Jiang, F. (2024). A Biomimetic "Salting Out-Alignmen-Locking" Tactic to Design Strong and Tough Hydrogel. Adv. Mater. *36*, e2400084. https://doi.org/10.1002/adma.202400084.
36. Zhong, D., Wang, Z., Xu, J., Liu, J., Xiao, R., Qu, S., and Yang, W. (2024). A strategy for tough and fatigue-resistant hydrogels via loose cross-linking and dense dehydration-induced entanglements. Nat. Commun. *15*, 5896. https://doi.org/10.1038/s41467-024-50364-3.
37. Collewijn, H. (1977). Eye- and head movements in freely moving rabbits. J. Physiol. *266*, 471–498. https://doi.org/10.1113/jphysiol.1977.sp011778.
38. Demer, J.L. (2015). Compartmentalization of extraocular muscle function. Eye (Lond) *29*, 157–162. https://doi.org/10.1038/eye.2014.246.
39. Lloyd, E.C., Dhakal, S., Amini, S., Alhasan, R., Fratzl, P., Tree, D.R., Morozova, S., and Hickey, R.J. (2025). Porous hierarchically ordered hydrogels demonstrating structurally dependent mechanical properties. Nat. Commun. *16*, 3792. https://doi.org/10.1038/s41467-025-59171-w.
40. Neumann, M., di Marco, G., Iudin, D., Viola, M., van Nostrum, C.F., van Ravensteijn, B.G.P., and Vermonden, T. (2023). Stimuli-Responsive Hydrogels: The Dynamic Smart Biomaterials of Tomorrow. Macromolecules *56*, 8377–8392. https://doi.org/10.1021/acs.macromol.3c00967.
41. Banerjee, H., Suhail, M., and Ren, H. (2018). Hydrogel Actuators and Sensors for Biomedical Soft Robots: Brief Overview with Impending Challenges. Biomimetics (Basel) *3*, 15. https://doi.org/10.3390/biomimetics3030015.
42. Dong, C., and Malliaras, G.G. (2025). Recent Advances in Stimuli-Responsive Materials and Soft Robotic Actuators for Bioelectronic Medicine. Adv. Mater. *37*, e2417325. https://doi.org/10.1002/adma.202417325.
43. Carton, F., Rizzi, M., Canciani, E., Sieve, G., Di Francesco, D., Casarella, S., Di Nunno, L., and Boccafoschi, F. (2024). Use of Hydrogels in Regenerative Medicine: Focus on Mechanical Properties. Int. J. Mol. Sci. *25*, 11426. https://doi.org/10.3390/ijms252111426.
44. Saeed, S., Khan, S.U., Khan, A.J., Ullah, M., and Gouda, M.M. (2025). Recent advances in biomimetic hydrogel materials for cardiac medicine applications. Discov. Mater. *5*, 239. https://doi.org/10.1007/s43939-025-00440-2.
45. Zhu, H., Wang, C., Yang, Y., Ma, H., Fan, X., Zhang, Y., Dai, Z., Cai, R., and Qian, K. (2025). High-strength mechanically gradient hydrogels via physical crosslinking for tendon-mimetic tissue repair. npj Flex. Electron. *9*, 53. https://doi.org/10.1038/s41528-025-00430-7.
46. Babaahmadi, M., and Yeganeh, H. (2023). Poly(vinyl alcohol)-gelatin crosslinked by silane-functionalized guanidyl-hydroxyurethane oligomer as contact-killing non-leaching antibacterial wound dressings. Biomed. Mater. *18*, 045011. https://doi.org/10.1088/1748-605X/acd5a0.
47. Hoyle, C.E., and Bowman, C.N. (2010). Thiol–Ene Click Chemistry. Angew. Chem. Int. Ed. Engl. *49*, 1540–1573. https://doi.org/10.1002/anie.200903924.
48. Lake, G.J., and Thomas, A.G. (1967). The strength of highly elastic materials. Proc. R. Soc. Lond. A *300*, 108–119. https://doi.org/10.1098/rspa.1967.0160.
49. Bai, R., Yang, J., Morelle, X.P., Yang, C., and Suo, Z. (2018). Fatigue Fracture of Self-Recovery Hydrogels. ACS Macro Lett *7*, 312–317. https://doi.org/10.1021/acsmacrolett.8b00045.
50. Ogden, R.W. (1972). Large deformation isotropic elasticity – on the correlation of theory and experiment for incompressible rubberlike solids. Proc. R. Soc. Lond. A *326*, 565–584. https://doi.org/10.1098/rspa.1972.0026.
51. Jablonská, E., Kubásek, J., Vojtěch, D., Ruml, T., and Lipov, J. (2021). Test conditions can significantly affect the results of in vitro cytotoxicity testing of degradable metallic biomaterials. Sci. Rep. *11*, 6628. https://doi.org/10.1038/s41598-021-85019-6.
52. Keenan, C.M., Baker, J.F., Bradley, A.E., Goodman, D.G., Harada, T., Herbert, R., Kaufmann, W., Kellner, R., Mahler, B., Meseck, E., et al. (2015). International Harmonization of Nomenclature and Diagnostic Criteria (INHAND) progress to date and future plans. J. Toxicol. Pathol. *28*, 51–53. https://doi.org/10.1293/tox.2014-0049.